Instability of Thin Films

From Fluids to Solids

P. Damman

Laboratoire Interfaces & Fluides Complexes
Université de Mons
20, Place du Parc, 7000 Mons, Belgique

Acknowledgements

Contents

1

Introduction

When speaking about thin films, I like to start with the aesthetic bursting of viscous bubbles. In a single experiment, you can follow the opening dynamics of a hole in a viscous thin film of fluid and the buckling of a thin sheet.
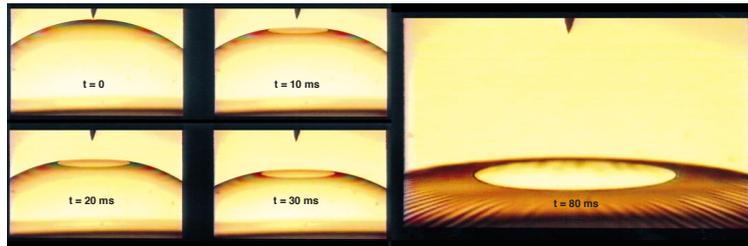

Fig. 1.1 Bursting of a viscous bubble of polydimethylsiloxane from (Debregeas et al. 1998).

The dynamics of hole opening is determined by a balance of capillary forces and viscous dissipation within the fluid film, the radial wrinkles observed in final stages correspond to the buckling of the collapsed bubble.

This example beautifully shows that tiny mechanical or capillary forces can destabilize the homogeneous flat state of a thin film leading to the growth of complex shapes and patterns. Experimental and theoretical studies on pattern formation are driven by the desire to understand the fundamental mechanisms by which such forces can lead to the spontaneous formation of multi-scale structures via symmetry breaking processes. This understanding is fundamental to envision applications in various domains such as micro and nanofluidics, flexible electronics, and the development of new surface-pattering technologies .

In the following, we will first discuss the stability of liquid films, thinner than 1 μm, deposited on solid surfaces with an emphasis on the nature of intermolecular forces and thermal fluctuations that conspire to generate complex morphologies. We will see how the global dewetting dynamics is driven by the solid-fluid interface and that dewetting can be a powerful tool to study the nano-rheology of complex fluids, such as polymer melts, in ultra thin films.

In the second part, we will consider thin elastic sheets constrained by mechanical forces. The canonical example of such system is given by a simple paper ball. We will see how the global geometry of these constraints drastically affects the final shape adopted by the sheet.

2
Films of Fluids

When a liquid is deposited on a solid surface, two situations can be observed. The fluid can form a continuous film that perfectly wets the substrate or can be fragmented in drops and droplets with a well defined contact angle. This contact angle, θ, is determined by a balance of forces at the three phase contact line which yields the Yound-Dupré relation (de Gennes et al. 2003).

$$\gamma_L \cos\theta = \gamma_S - \gamma_{SL}$$

with γ_L, γ_S, and γ_{SL} the free surface energy related to the liquid-air, solid-air and solid-liquid interfaces.

The ability of a liquid to wet a surface is usually described with the spreading parameter, $S = \gamma_S - (\gamma_{SL} + \gamma_L)$. If $S < 0$, the liquid form droplets, we are in partial wetting. By using spin-coating, it is however possible to "force" the liquid to wet the solid surfaces even in partial wetting regime. The resulting liquid film is then unstable and tends to spontaneously desegregate to form collections of droplets, this transition is called dewetting. Interestingly, the mechanisms of dewetting depends on the film thickness (Bonn et al. 2009). In partial wetting conditions, the film destabilize to expose "dry" patches, unless it is sufficiently thick to be stabilized by gravity. For relatively thick films, the system is perturbed by the presence of surface heterogeneities or dust particles, which form the initial nucleus for a hole. Dewetting proceeds via a nucleation-growth mechanisms (i.e., heterogeneous nucleation) (Fig 2.1). In contrast, if the nucleation is induced by thermal fluctuations, nucleation is homogeneous. This is observed for very thin films 210 nm when long-range forces become significant. The system can become linearly unstable, so the growth of thermal fluctuations leads to spontaneous destabilization (Fig 2.1). This scenario has been called spinodal dewetting, in analogy to the spontaneous decomposition of incompatible bulk phases (Reiter 1992; Bonn et al. 2009; Baumchen et al. 2003).

The free energy of film $F(h)$ can explain the co-existence of these two mechanisms (de Gennes et al. 2003). This free energy including gravity, surface energy and long range van der Waals forces, is given by

$$F(h) = \gamma_{SL} + \gamma_L + \frac{1}{2}\rho g h^2 + P(h)$$

The long range free energy is determined by the Hamaker constant, H via the relation $P(h) = -H/12\pi h^2$, obtained by summing all atom-atom attractive contributions ($\sim -1/r^6$). The Hamaker constant ranges between 10^{-18} and 10^{-21} J, for high energy and low-energy organic surfaces, respectively (in the studies reported here,
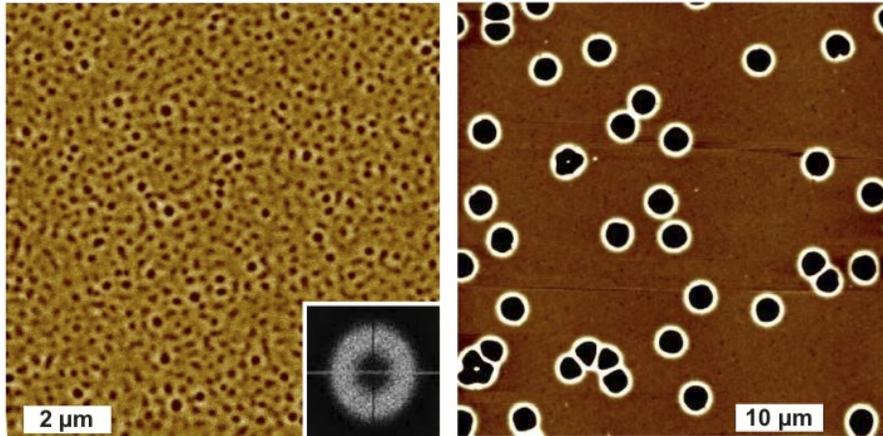
Fig. 2.1 (left) Labyrinthine or spinodal dewetting and (right) nucleation-growth pattern (Baumchen et al. 2010).

we only consider positive Hamaker constants). As shown in Fig 2.2, a Maxwell construction shows two transitions mechanism (similar to the VdW liquid-gas transition). The instability domain is related to the spinodal dewetting while the metastable one corresponds to the nucleation-growth mode.
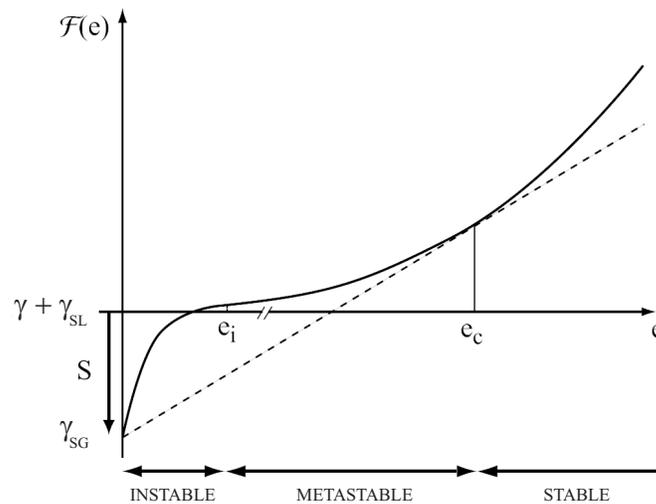

Fig. 2.2 Evolution of the free energy of a thin film of fluid with thickness.

The two mechanisms generate different patterns, i.e., a characteristic wavelength for spinodal, a well-defined holes opening dynamics for nucleation-growth regime. These mechanisms can be qualitatively (and quantitatively) understood from scaling

law theoretical models.

2.1 Spinodal Dewetting

For temperatures higher than absolute zero, the free surface of a liquid is always disturbed by thermal capillary waves. These waves are characterized by a superposition of various independent modes described by a continuous spectra, relating their amplitude A to their wavenumber, q. We consider each mode disturbing the fluid-air interface, $\zeta(r) = A(q)\cos qr$ separately. The free energy can be adequately described by considering gravity and capillarity.

$$U = \int \left[\frac{1}{2}\rho g \zeta^2 + \gamma \left(1 + (\partial_x\zeta)^2 + (\partial_y\zeta)^2\right)^{1/2} \right] \, dx \, dy \qquad (2.1)$$

$$\simeq \int \left[\frac{1}{2}\rho g \zeta^2 + \gamma \left(1 + \frac{1}{2}(\partial_x\zeta)^2 + \frac{1}{2}(\partial_y\zeta)^2\right) \right] \, dx \, dy \qquad (2.2)$$

The excess energy due to this perturbation is given by

$$\Delta U_q \simeq \left[\frac{\rho g}{2}A^2 + \frac{\gamma}{2}A^2 q^2 \right] L^2$$

The spectra A^2 can now be derived by considering the equipartition theorem, the average energy of one mode is equal to kT

$$A(q)^2 = \frac{kT}{\rho g + \gamma q^2} \qquad (2.3)$$

Experimental observations of thermal waves by scattering methods, x-ray, neutron reflectivity (via the extent of interfacial roughness) or by direct inspection of "frozen" surfaces of glassy materials with atomic force microscopy agree well with the q^{-2} law (eq 2.3) (Sferraza et al. 1997, Coppée et al. 2004).

For very thin films ($h < 100$ nm) undergoing spinodal dewetting, an additional energy term corresponding to the interaction between air-fluid and fluid-solid interfaces should be considered. To understand the stability of such thin films, long range VdW forces should be added in the model. Neglecting gravity, the free energy of a perturbed film surface ($h \rightarrow h + u$) is given by

$$F = \int dx \, dy \left[\frac{\gamma}{2}(\nabla h)^2 + P(h + u) \right] \qquad (2.4)$$

Expanding $P(h + u)$ yields

$$\delta F = \int dx \, dy \left[\frac{\gamma}{2}(\nabla u)^2 + \frac{1}{2} P''(h) \, u^2 \right] \qquad (2.5)$$
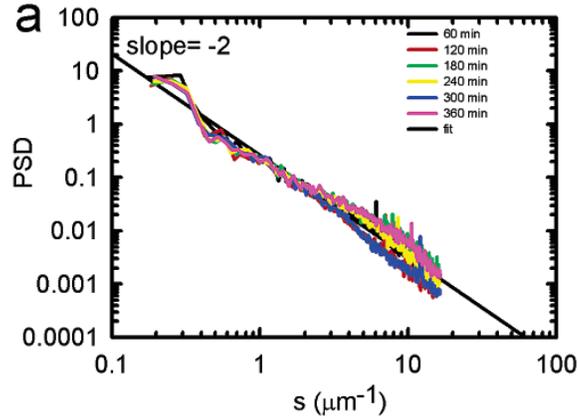
With $P''(h) = -H/2\pi h^4$

Fig. 2.3 Evolution of the power spectral density ($PSD \equiv A^2$) computed from AFM images recorded for a "frozen" surface of random PET copolymer, $T_g \simeq 80°C$ (Coppée et al. 2004).

Considering a periodic perturbation $u(r,t) = u_q \cos qr \; e^{t/\tau}$, the excess free energy becomes

$$\delta F_q = \left[\frac{\gamma}{2} q^2 - \frac{H}{4\pi \; h^4} \right] u_q^2 \tag{2.6}$$

For $H < 0$ the film is stable against all perturbation, for $H > 0$, the film surface is unstable face to wavenumber smaller than a critical wavenumber q_c deduced from Eq 2.6

$$q_c \sim \left(\frac{H}{\gamma} \right)^{1/2} h^2 = \frac{h^2}{\ell}$$

(usually $\ell \simeq 1nm$).

The observed wavelength corresponds to the fastest mode, considering viscous dissipation in the flow required to accommodate the perturbation of the fluid interface. In the lubrication approximation, the viscous dissipation is given by (de Gennes et al. 2003)

$$T\Delta\dot{S} = \int \eta \left(\frac{\partial v}{\partial x} \right)^2 \sim \eta \frac{v_x^2}{h^2} h \tag{2.7}$$

Considering volume conservation ($div\vec{v} = 0$, $v_x/\lambda \sim \dot{u}/h$), we have

$$\left[\gamma q^2 - \frac{H}{4\pi \; h^4} \right] u\dot{u} = -\eta \frac{\dot{u}^2}{h^3 q^2} \tag{2.8}$$

Solving this equation for $u = u_0 \; e^{t/\tau}$ yields the dispersion curve relating the growth rate $1/\tau$ and wavenumber q

$$\frac{1}{\tau} = -\frac{\gamma}{\eta} h^3 q^2 \left(q^2 - \frac{H}{4\pi\gamma \; h^4} \right) \tag{2.9}$$
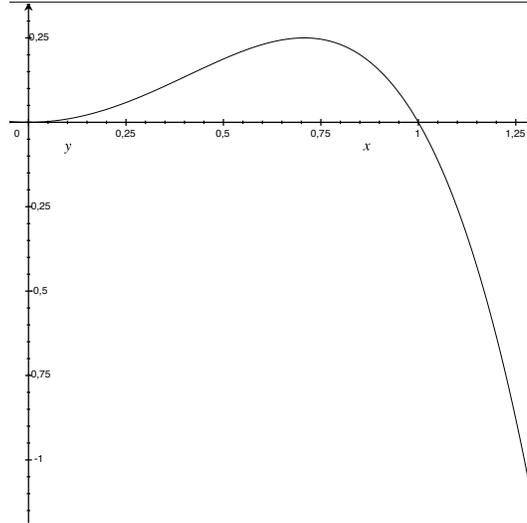
Fig. 2.4 Evolution of the growth rate $1/\tau$ with the wavenumber q from Eq 2.9. Unstable modes corresponds to positive value of $1/\tau$ ($0 < q < q_c$), the fastest mode q_F being obtained by maximizing the growth rate.

The wavelength and latent time of the fastest mode are,

$$q_F = \frac{1}{\sqrt{2}}\left(\frac{H}{4\pi\gamma\ h^4}\right)^{1/2} = \frac{1}{\sqrt{2}}q_c \quad \text{and} \quad \tau_F \sim \frac{\eta\ \gamma}{H^2}\ h^5 \qquad (2.10)$$

This rather crude model predicts a wavelength $\lambda \sim h^2$ (a density of holes $N \sim 1/\lambda^2 \sim h^{-4}$) in close agreement with experimental observations for a large variety of samples (Fig 2.5). Interestingly, the observed wavelength can be used to estimate important data for interfacial phenomena, i.e., the Hamaker constant, H and/or the interfacial free energy γ (see eq 2.10). Obviously, this is only valid for the first stages of the dewetting since a coarsening of the pattern is observed due to the coalescence of tiny holes into larger ones. Similarly, changing the environment of the fluid (replacing air by another fluid for instance) will drastically affect the wavelength of the spinodal dewetting (Reiter et al. 2000).

For nanometric thin films, the long range VdW forces favor spinodal dewetting and the emergence of a labyrinthine pattern with a specific wavelength. In contrast, for very thick films ($h \gg 1\mu m$), a continuous spectra of modes disturb the air-fluid interfaces (i.e., the thermal capillary waves).

2.2   Dewetting by nucleation and growth

As shown in the previous section, spinodal dewetting cannot be observed for thick films. If the spreading parameter is negative, the "forced" fluid will break with a nucleation mechanisms. As other phase transitions, the nucleation of holes in a liquid film can be homogeneous (very rare) or heterogeneous (by far most frequent). In the
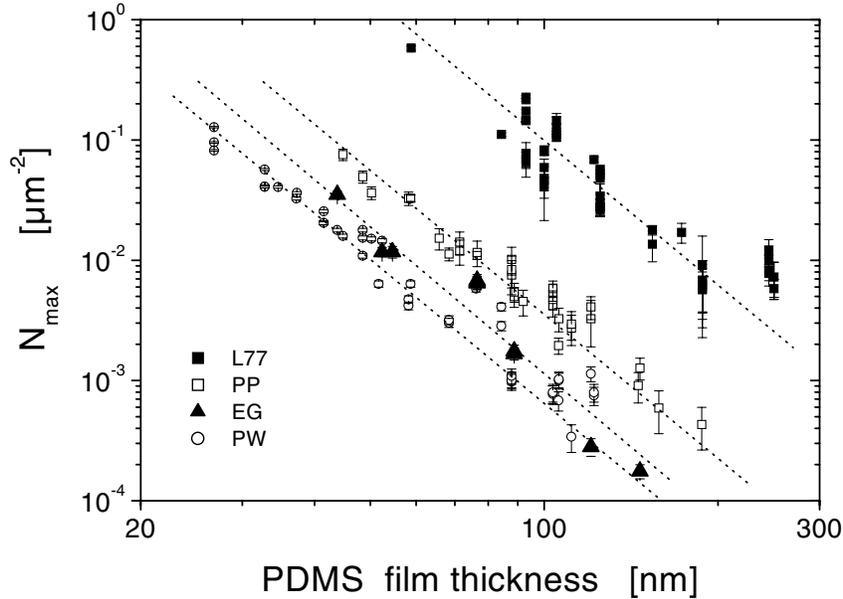
Fig. 2.5 Evolution of the density of holes vs film thickness for polydimethylsiloxane thin films in various environments water (PW), ethylene glycol (EG) and a surfactant (L77) see (Reiter et al. 2000) for details. The dotted lines correspond to h^{-4} laws.

following, we will not discuss the nucleation stage but focus instead on the dynamics of hole opening. This dynamics is indeed directly related to the internal properties of the fluid and to the boundary condition for the flow at the buried fluid-solid interface.

For relatively thick films of Newtonian fluids, such as PDMS oil, (we will see later what means "thick"), the holes open with a constant velocity, independent of the film thickness. As shown by Brochard-Wyart, this constant opening velocity can be adequately described by a balance of capillary energy gained by dewetting ($S = \gamma_S - (\gamma_{SL} + \gamma_L)$) and viscous dissipation in the rim wedge (Redon et al. 1991)

$$V \sim \frac{\gamma}{\eta}\theta^3 \tag{2.11}$$

For thin films of complex fluid such a a polymer melts, completely different behaviors are observed. The opening velocities strongly depend on the film thickness and decrease gradually with time according a well-defined power law $V \propto t^{-1/3}$ (reiter et al. 2000b; Damman et al. 2003; Gabriele et al. 2006). This behavior cannot be understood by considering the energy dissipation within a flow through the whole film (which yields a constant velocity). It was however suggested by de Gennes (1985) that polymer melts could slip at repulsive solid surfaces (Fig 2.6). This slippage can be quantified with the slippage length determined by a balance of friction and shear stress at the solid-fluid interface.

$$\sigma_f = kV_s = \sigma_v^i = \eta \ \left(\frac{\partial v_x}{\partial z}\right)_{z=0} \simeq \eta \frac{V_s}{b} \tag{2.12}$$

where η, k, and b are the viscosity, the friction coefficient and the slippage length, respectively.

Interestingly, we are now able to determine when a film of fluid is "thick" ($h \gg b$) or "thin" ($h \ll b$). The dissipation mechanisms are characterized by different boundary conditions, no-slip for thick films (viscous flow dissipation) and full-slip for thin ones (friction at fluid-solid interface).
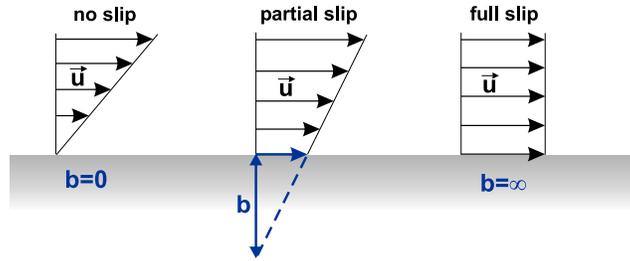

Fig. 2.6 Scheme slip vs no-slip boundary conditions

For entangled polymer melts, the viscosity is given by the reptation model (Rubinstein et al. 2003). Considering the diffusion of the polymer chain through its tube, made by the entanglements with neighboring chains, we obtain the viscosity,

$$\eta \sim \frac{\zeta}{a} \frac{N^3}{N_e^2} \tag{2.13}$$

Where a, N_e, ζ, N are the monomer size, the number of chain segments between two entanglements, the monomer friction coefficient and the number of segments in the whole chain, respectively.

The friction coefficient k can be easily related to the monomer friction coefficient with the relation $k \sim \zeta/a^2$. With these relations, we can show that the slippage length for entangled polymer melts is given by,

$$b = a^2 \ \frac{\eta}{\zeta} \sim a \ \frac{N^3}{N_e^2} \tag{2.14}$$

As shown in Fig 2.8, the observed slippage length agree well with this law in principle valid for chains on a perfectly repulsive surface. Due to the entanglements, very large slippage length are observed for polymer melts. For example, a polystyrene, PS, melt of very large chains ($M_w = 10^6 Da$) has a slippage length exceeding one centimeter ! In contrast, slippage lengths observed for small molecules are nanometric and barely exceeds a few molecular sizes (Bocquet et al. 2010).

This drastic change of the boundary conditions at the solid-fluid interface have a strong impact on dewetting dynamics. For the opening of holes in viscous bubbles,
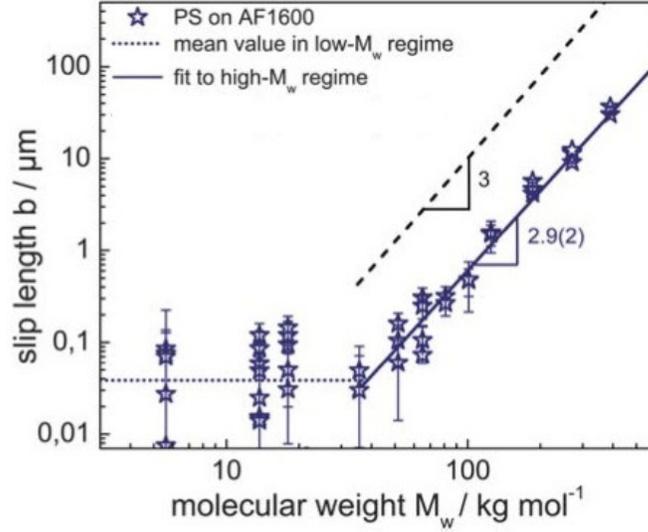
Fig. 2.7 Evolution of slippage length with molecular weight (Baumchen et al. 2009).

the capillary stress at the edge of the hole propagates throughout the entire fluid films (Debregeas et al. 1998). In contrast, for a viscous film on a solid substrate, the capillary stress will propagate on a much smaller distance, determined by the slippage length (or the friction at the fluid-solid interface). Balancing friction and viscous forces (for large slippage length, we can assume a plug flow: $\sigma_x \sim \eta \partial_x V_x$) yields a differential equation (Vilmin et al. 2006, Vilmin 2006)

$$kV_x \sim h_0 \partial_x(\sigma_x) = \eta h_0 \partial_{xx} V_x$$

Solving this ODE shows that the velocity field exponentially decays from the dewetted edge with a characteristic length-scale, $\Delta = \sqrt{bh_0}$

$$v(x,t) = V \ \exp\left(-\frac{x - L(t)}{\Delta}\right) \tag{2.15}$$

where $L(t)$ is the dewetted distance.

Due to the friction of the fluid at the solid surface, there is a minimum size for the rim $\Delta \sim \sqrt{bh}$, even for the very initial stages of dewetting.

For polymer melts in thin films ($h \ll b$), the dynamics of hole opening is thus given by a balance of capillary power gained by dewetting (SV) and the energy dissipated by the friction of the moving rim (kWV^2).

$$S \ V \sim \frac{\eta}{b} W \ V^2 \quad \text{and} \quad V = \frac{Sb}{\eta} W^{-1} \tag{2.16}$$

where S, V, and W are the spreading parameter, the dewetting velocity and the rim width ($k = \eta/b$).

The rapid decrease of dewetting velocity when the rim width increases ($V \propto 1/W$) is a signature of the slippage mechanisms. For dissipation in a purely viscous flow in the rim wedge, the velocity is insensitive to the rim width (and the film thickness) (Redon et al. 1991).

The global dynamics can be easily obtained from volume conservation, the dewetted fluid should be in the rim $hD \sim \theta W^2$. We obtain,

$$\frac{dD}{dt} = \frac{Sb}{\eta} \frac{\theta}{\sqrt{hD}} \tag{2.17}$$

where D is the dewetted distance.

Solving this equation fully characterize the dewetting dynamics,

$$D(t) \sim \left(\frac{\gamma\theta^{5/2}}{\eta h^{1/2}}\right)^{2/3} b^{2/3} t^{2/3} \tag{2.18}$$

$$V \sim \left(\frac{S\theta}{k\sqrt{h}}\right)^{2/3} t^{-1/3} \tag{2.19}$$

$$W(t) \sim \left(\frac{\gamma\theta h}{\eta}\right)^{1/3} b^{1/3} t^{1/3} \tag{2.20}$$

$$b \sim \frac{\eta}{\gamma\theta^2} \left(\frac{D(t)W(t)}{t}\right) \tag{2.21}$$

These relations are in close agreement with the dewetting dynamics observed for various polymers (Fig 2.8). The last relation also suggests that the slippage length can be easily estimated from the dewetting data (Reiter et al. 2000).

2.3 Viscoelasticity

In the previous section, we discussed the dewetting dynamics for purely viscous polymer melts (i.e., very small Deborah numbers, $De \ll 1$). This behavior is usually observed at temperatures well above the glass transition temperature, such as room temperature experiments with PDMS, $Tg \simeq 150K$. It can be however interesting to adjust the dewetting temperature to follow the elastic - viscous transition which occurs at the reptation time ($De \simeq 1$). Indeed, slightly above T_g, the elastic/rubber state of the polymer melt extents over large time intervals, for PS $T_g \simeq 373K$. To describe the dynamics of entangled polymer melts, two characteristic times are used the entanglement time, τ_E and disentanglement/reptation time, τ_{rep}. We will focus our discussion on the reptation time corresponding to the elastic-viscous transition. Due to entanglements, the reptation time is a strong function of the chain length (or the molecular weight) and is given by the relation (Rubinstein et al. 2003),

$$\tau_{rep} \sim \frac{\zeta a^2}{kT} N_e^2 \left(\frac{N}{N_e}\right)^3 \tag{2.22}$$

The temperature dependence of the relaxation times, related to friction coefficient ζ, is usually accounted for by using the William-Landel-Ferry relation. This
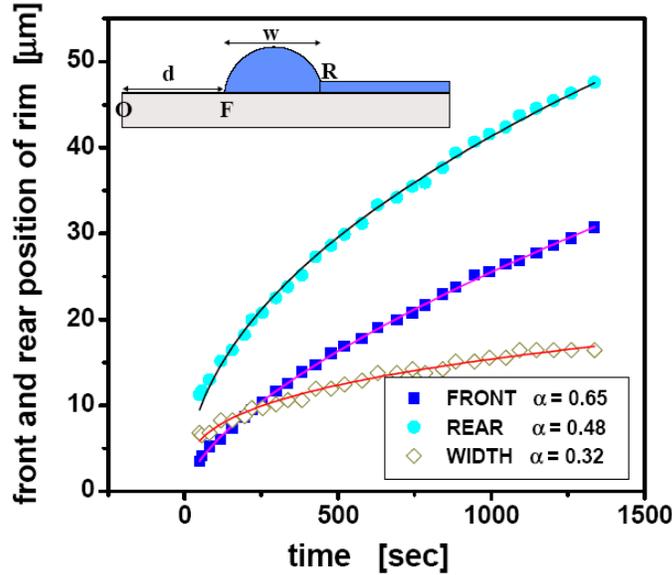
Fig. 2.8 Dewetting dynamics for PDMS on Si wafer coated with PDMS brushes (Reiter et al. 2000).

(quasi)universal law gives an estimate of the a_T coefficient used to re-scale the experimental curves (with T_g as reference temperature).

$$a_T = \frac{\tau(T)}{\tau(T_G)} \exp\left(-17.4 \frac{(T - T_G)}{(T - (T_G - 51.6K))}\right) \tag{2.23}$$

The dewetting of PS at temperatures close to T_g thus reveals the occurrence of two well defined morphologies for the rim collecting the dewetted fluid. For short times ($t \ll \tau_{rep}$), when PS behaves as a purely elastic material, asymmetric rims shapes are observed with an exponential decay morphology (Fig 2.9) that can be related to the interfacial slippage (Vilmin et al. 2006). For long times ($t \gg \tau_{rep}$), equilibrated rim with a round shape are observed. This cylindrical rim morphology equilibrates the Laplace pressure within the fluid in motion. This rounded morphology is usually observed for purely viscous fluids in the mature regime (already discussed in the previous section).

The dewetting dynamics of PS at temperature close to T_g also show different regimes. From the evolution of dewetted distance with time, Fig 2.10, three regimes can be observed, i) constant velocity, ii) decrease of velocity with time ($t^{-1/2}$) followed by a change of slope indicating iii) a shallower decrease of velocity ($t^{-1/3}$). Interestingly, the first two regimes ($V \propto t^0$, $V \propto t^{-1/2}$) are independent of the M_w, while the last one ($V \propto t^{-1/3}$) exhibits a strong influence of chain length (Damman et al. 2007). These regimes are related to the two major relaxation times, τ_e and τ_{rep}. The short relaxation time τ_e corresponds to the Rouse dynamics of single strands between entanglements, the melt behaves like a viscous fluid (of very low viscosity). Since the
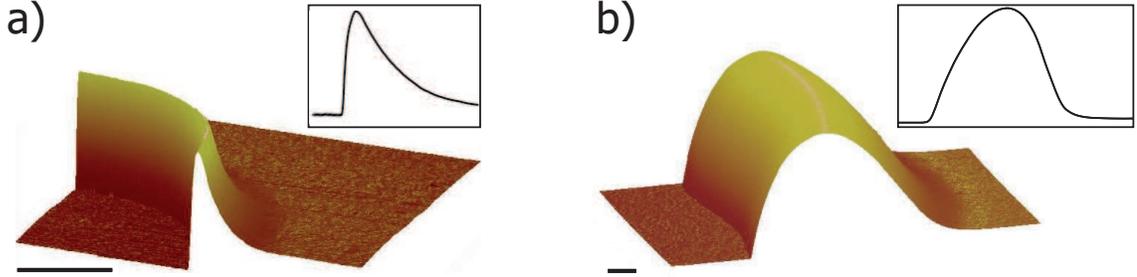
a)

b)

Fig. 2.9 Short (a) and long (b) time morphology of the rim collecting the liquid for a high molecular weight PS close to the glass transition.
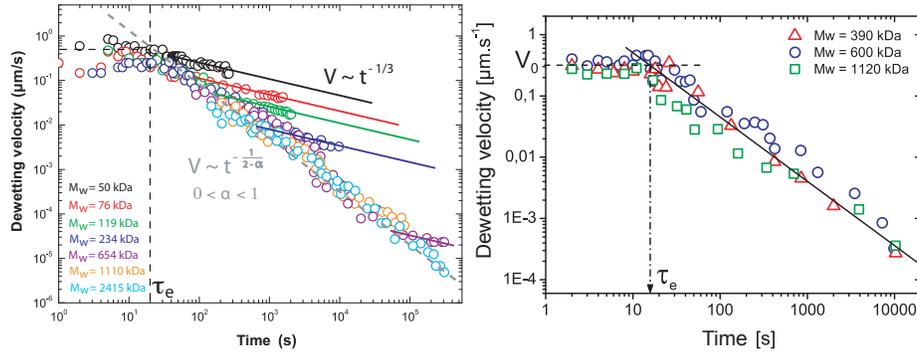

Fig. 2.10 Dewetting dynamics, evolution of the dewetted distance for PS at temperature close to T_g ($T \sim 400K$). As indicated.

density of entanglements is constant, τ_e is independent of the chain length. The long relaxation time τ_{rep} corresponds to the time required for the chain to escape from the tube or to disentangle from other chains. The length of the tube is determined by the density of entanglements and the chain length, τ_{rep} thus strongly varies with the molecular weigth ($\tau_{rep} \propto N^3$).

For very short times $t < \tau_e$ (for PS at dewetting temperatures, $\tau_e \sim 1s$), the melt behaves as a fluid of low viscosity η_i. Very large dewetting velocity is then expected, and can be related to the monomer viscosity and moderate slippage length. As for viscous fluids, we assume a balance of capillary and friction at solid-fluid interface, equ 2.16,

$$V_i \sim \frac{S}{k}\Delta_i^{-1} = \frac{S}{\sqrt{kh}\ \eta_i}$$

For intermediate times $\tau_e < t < \tau_{rep}$, the rheology of melt is dominated by elasticity. We thus assume that the polymer behaves as a true elastomer (Damman et al. 2007). The capillary stress at the three phase contact line $\sigma \sim S/h$ generates a strain given by the relation

$$\frac{S}{h} \sim E\frac{(H-h)}{h} \simeq E\frac{H}{h}$$

where S, E, H, h are the spreading parameter, the plateau elastic modulus, the actual and initial film thicknesses.

The observation of a constant film thickness during the elastic plateau agrees with a maximum of deformation and supports this assumption (Fig 2.11 (a)).
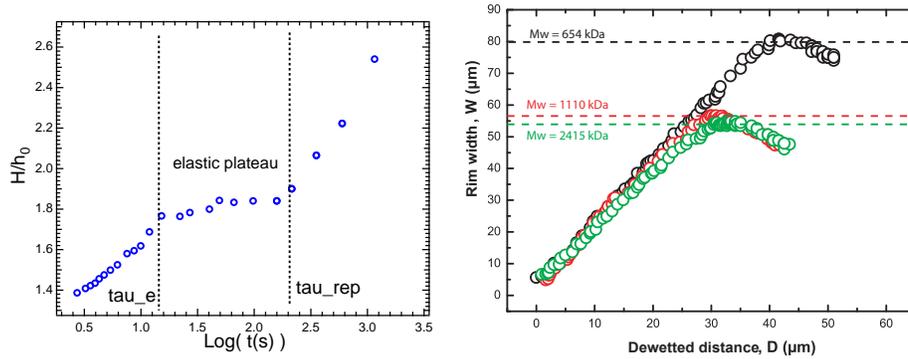

Fig. 2.11 (a) Evolution of the maximum rim height, H with time for a PS melt at temperature close to T_g ($M_w = 100k$, $T \sim 400K$, $h \sim 100nm$). (b) Evolution of the rim width with the dewetted distance.

The volume conservation of the dewetted fluid yields the relation

$$h_0 D \sim WH \simeq W\frac{S}{E} \tag{2.24}$$

$$W \sim \frac{Eh_0}{S}D \tag{2.25}$$

The linear dependance of the rim width with the dewetted distance is perfectly supported by various experimental observations in the plateau regime, see Fig 2.11 (b). For such polymer melt in a rubber state, we expect a very large slippage length ($b = \eta/k \simeq \infty$). The dewetting velocity is then determined by a balance of capillarity gain vs friction dissipation, $V \sim S/k \ W^{-1}$. Combining this relation with the volume conservation, the velocity is expected to decrease as $t^{-1/2}$ during all the plateau elastic regime, in close agreement with the experimental observations (Fig 2.10).

$$V \sim \left(\frac{S}{\sqrt{kEh_0}}\right) t^{-1/2} \tag{2.26}$$

For very long times $\tau_{rep} < t$, the melt flows like a highly viscous fluid $\eta \gg \eta_i$, its viscosity being determined by the relaxation of entanglements ($\eta \sim E\tau_{rep}$). The dewetting dynamics of such a viscous fluid on a slippery surface was described in the previous section, and is given by the relation,

$$S \ V \sim \frac{\eta}{b}W \ V^2, \qquad V = \frac{Sb}{\eta}W^{-1} \quad \text{and} \quad V \sim \left(\frac{S\theta}{k\sqrt{h}}\right)^{2/3} t^{-1/3} \tag{2.27}$$

The predicted decrease of dewetting velocity according $t^{-1/3}$ is in agreement with experimental observations. At the transition between elastic and viscous regime, both velocities should be equal,

$$\frac{S}{\sqrt{kh_0}}\eta^{-1/2} \sim \left(\frac{S}{\sqrt{kEh_0}}\right)\tau_{rep}^{-1/2} \tag{2.28}$$

This equation can be easily re-organized to yield the classical relation for viscoelastic fluids, $\eta \sim E\tau_{rep}$ showing the self-consistency of the model.

The elastic - slippage model can be tested by using the dependence of viscosity with temperature and M_W since the maximum viscous dewetting velocity (V_{max} at the elastic-viscous transition) is given by,

$$V_{max} \sim \frac{S}{k}\Delta^{-1} = \frac{S}{\sqrt{kh}}\eta^{-1/2} \propto M_w^{-3/2}\, a_T^{-1/2} \tag{2.29}$$

With these relations, all the data collapse on master curves, V/V_{max} vs time (Fig 2.12).
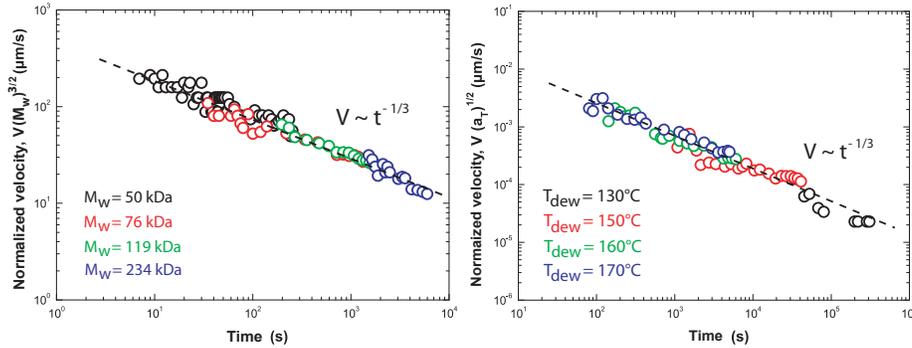

Fig. 2.12 Master curve obtained for the dewetting velocity for various PS at different temperatures. The normalized velocity are obtained with the relation $V_{max} \propto M_w^{-3/2}\, a_T^{-1/2}$. Normalization of temperatures was achieved with the a_T parameter (see text).

2.4 Conclusions - Nano-rheology

The model based on the elastic-viscous transition is a very powerful tool to study the rheology of strongly confined fluids. The very large slippage length associated to long polymer chains, that can be as large as one centimeter, enhances the minute modifications in the fluid or at the interface (Coppée et al. 2011). From the dewetting dynamics recorded with various experimental conditions, the evolution of the reptation time with temperature and molecular weigh can be obtained for thin films $\sim 100nm$ thick (Fig 2.13). Interestingly, the observed reptation times follow the bulk behavior $\tau_{rep} \propto a_T$ and $\tau_{rep} \propto M_W^{3.4}$. The adequacy between bulk and confined chain dynamics clearly shows that confinement has no influence on the collective dynamics of chains (at least for $h \simeq 100nm$, for comparison $10 < R_g < 200nm$ for the studied chains).
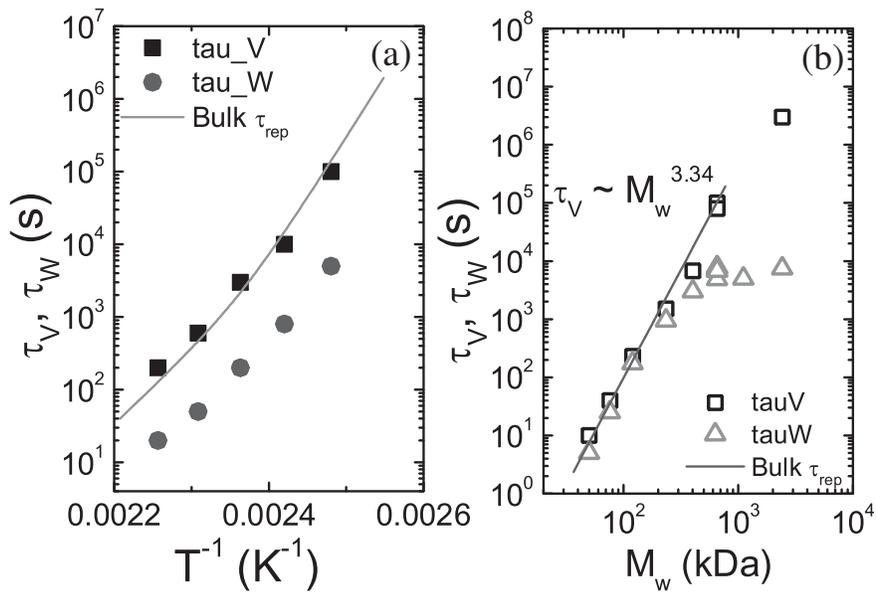
Fig. 2.13 Evolution of reptation times measured at the dewetting transition with temperature and molecular weight. The solid lines represent data from classical rheological measurements (Damman et al. 2007).

3
Stability of thin sheets

Homogeneous states of constrained thin sheets are very often unstable. Their final states can exhibit a zoo of complex morphologies made of wrinkles, creases, crumples, folds, and blisters, several morphologies sometimes co-existing in a single experiments. Transition from one morphology to another can be observed depending on various experimental conditions. For instance, by decreasing adhesion, you switch from regular wrinkles to blister. Increasing compression could also reveal nonlinear regimes with increasing complexity. As fluids, thin elastic sheets appears to be very promising systems that bear similarity with classical problems of linear and nonlinear pattern formation such as period-doubling bifurcations, Fig 3.1. Their study open new prospects to understand the emergence of complexity, breaking of symmetry and singularities.

Even the buckling of a sheet shows intrinsic behaviors that raise fundamental questions such as, why do films become folded upon confinement whereas a thick slab of an identical material generates creases ? why does paper sheets crumple into singularities whereas rubber sheets would smoothly wrinkle ? Answering these questions (and many others) is important, first for our natural curiosity, and to understand the emergence of complex shapes and patterns in Nature. Understanding thin sheets behavior is also extremely important for many technological applications. The design of new materials combining extreme mechanics with optical, electronic or chemical properties is very often achieved with specific coatings on thin sheets. In this case, the failure of the coating, or even the thin sheet itself, should be avoided. The opposite is also true ! These complex features can be very interesting for some applications, essentially in micro- and nano-technology . Indeed, understanding how complex patterns emerge spontaneously under featureless forces may inspire efficient methods for tailoring a desired surface pattern to achieve the required property (e.g., reversible superhydrophoby, flexible electronics).

The energy of a thin sheet is usually described within the Foppl-von Karman approximation. It includes stretching and bending energy related to the different modes of deformation of the sheet, quantified by strains and curvatures.

$$U \sim Y(strain)^2 + B(curvature)^2$$

where $Y \sim Eh$ and $B \sim Eh^3$, E, h being the elastic modulus and sheet thickness, respectively.

For constrained thin sheets, e.g. a paper sheet confined in a sphere, the deformation energy can be distributed in pure stretching and/or pure bending modes. Considering an out-of-plane deformation (amplitude Z) of a sheet (size L), the balance of stretching and bending energy
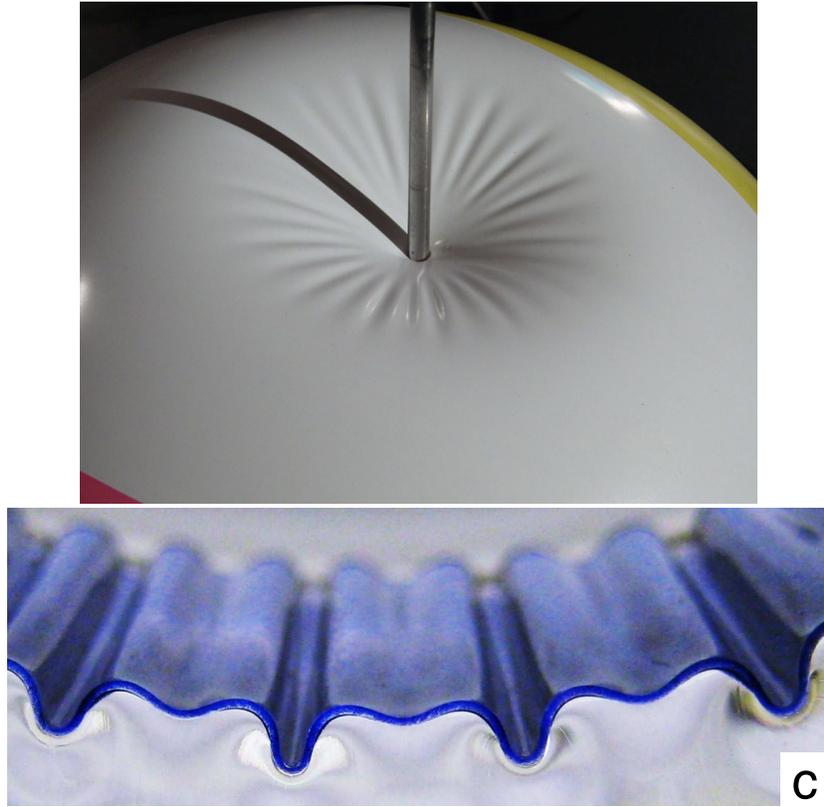
Fig. 3.1 Wrinkling pattern breaking the radial symmetry of an indented ball (Vella et al. 2011) and nonlinear wrinkling exhibiting a period-doubling bifurcation (Brau et al. 2010).

$$\frac{E_s}{E_b} \sim \frac{Y(Z/L)^4}{B(Z/L^2)^2} \sim \left(\frac{Z}{h}\right)^2$$

shows that pure bending mode is favored for large deformations ($Z \gg h$).

For bulk materials, this condition is clearly not fulfilled, this is why compressed bulk materials accommodate compression with pure stretching. The formation of creases at free surfaces, first described by Maurice Biot, can be however observed (Cai et al. 2012).

For thin sheets, the shapes that minimize energy should thus minimize stretching and according to the *Theorema Egregium* of C.F. Gauss, should avoid any change of metric, i.e. no change of Gauss curvature (Witten 2007, Audoly et al. 2010). In short, this theorem of differential geometry states why it is impossible to wrap a sphere with a flat surface without stretching !

3.1 Crumpling

Look at a paper ball, Fig 3.2, the compaction of this 2D paper sheet in a 3D sphere cannot be achieved with isometric transformations of the flat surface. This strong constraint obviously induces changes of Gauss curvature, at least locally. To minimize the energy, the sheet spontaneously adopts an origami-like configuration. As shown in Fig 3.3, the opened paper ball reveals a complex polygonal network of plane facets delimitated by sharp ridges (or tied folds) (Lobkovski et al. 1995, Blair et al. 2005). These ridges focus all the deformation energy of the sheet, the energy related to flat facets is negligible. These ridges can be considered as linear singularities.

Fig. 3.2 Morphology of a paper ball. Thin sheet confined in a sphere.

The ridges are connected each other by point-like singularities with a size comparable to the sheet thickness. As shown in Fig 3.4, the deformations involved into such a ridge contain bending and a non negligible amount of stretching (demonstrated by the deflection along the fold). The stretching is directly related to the change of fold width along the ridge, $\partial W/\partial x \sim w/L$. The maximum width of the ridge, w results from a balance of stretching and bending energy (Lobkovsky et al. 1995),

$$w \sim h^{1/3}L^{2/3}\alpha^{-1/3} \quad \text{and} \quad U \sim Eh^3 \left(\frac{L}{h}\right)^{1/3} \alpha^{7/3}$$

where L and α are the fold length and the angle between the planes delimiting the fold, respectively.

Interestingly, the width and energy of such a ridge are vanishing when the sheet thickness vanishes. The origami-model corresponds to zero thickness/zero energy morphology.

Fig. 3.3 Morphology of a paper ball. Opened paper ball showing the polygonal network morphology of ridges.

Fig. 3.4 The "bag shape" showing the morphology of a single ridge singularity.

3.2 Curtains

As discussed in the previous section, geometrically constrained thin sheets tend to adopt an origami-like morphology, as close as possible to isometric solutions including singularities. However, there could be specific geometrical constraints that are not compatible with such faceted morphology. As shown by mathematicians, an origami solution should follow some rules, i) the two colors rule, stating that no two colors can share a common face (or two colors are enough to colorize an origami), ii) the vertices follows the equation $m - v = \pm 2$ (m/v are the number of mountain/valley folds), iii) the sum of alternative angles around a vertex must be equal to π, and iv) the paper sheet cannot intersecting itself !

Thin sheets constrained at one edge and free at the other, i.e. a curtain-like morphology (Fig 3.5), develop a self-similar hierarchy of folds, a morphology that contradicts these rules (Huang et al. 2010, Vandeparre et al. 2011).
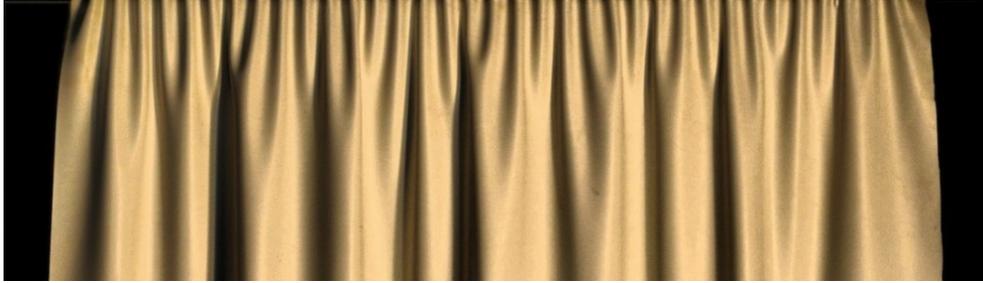
Fig. 3.5 Detail of a rubber curtain constrained at one edge with an imposed sinusoidal deformation $z(0, y) = A(0) \sin(q(0)y)$ (Vandeparre et al. 2011).
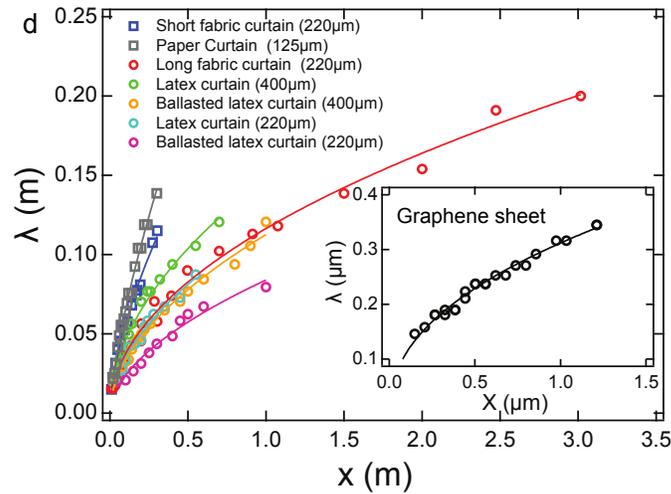

Fig. 3.6 Power laws describing the evolution of the wavelength with the distance from the constrained edge (Vandeparre et al. 2011).

As shown in Fig 3.5, sheets made of various materials constrained at one edge develop a hierarchical pattern of folds. These patterns consist of a hierarchy of successive generations of folds whose wavelength gradually increases along x. For the sake of clarity, the structure of the deformed sheet is described by a periodic function $z(x, y) = A(x) \sin q(x)y$, with z the amplitude of out-of-plane deflections, y being parallel to the edge ($q = 2\pi/\lambda$). To rationalize these various hierarchical patterns, we consider the evolution of the average wavelength, λ, with the distance to the constrained edge, x (Fig 3.6). For inextensible sheets, the amplitude of the folds is determined by the compression ratio and the inextensibility of the sheet, $A \sim \lambda \sqrt{\delta}$. Since, inextensibility ensures that

$$W_0 = \int_0^W ds \cos\theta \simeq \int_0^W ds \left(1 - \frac{1}{2}\dot{z}^2\right) \simeq W - \frac{1}{2}W\left(\frac{A}{\lambda}\right)^2$$

and $\delta = (W - W_0)/W$

The bending energy density related to a fold is thus given by

$$u_b \sim Eh^3 \, \kappa^2 \sim Eh^3 \delta / \lambda^2$$

Since u_b is proportional to $1/\lambda^2$, the membrane adopts the largest possible wavelength compatible with the imposed constraints. The minimization of bending energy is thus the "driving force" toward larger and larger folds and is the source of the observed hierarchy. Fig. 3.6 shows that the evolution of the average fold width, $< \lambda(x) >$ is adequately described by simple power laws, $< \lambda > \sim x^m$. Interestingly, curtains made of various materials with contrasted properties can be sorted in two classes with different exponents $\sim 2/3$ for "light" sheets and $\sim 1/2$ for "heavy" sheets (we will see later the meaning of light and heavy). We will now try to answer the questions, What energy terms do determine these exponents ? What processes do limit the evolution dynamics of fold width ?

To increase the wavelength, adjacent folds should merge. Looking carefully a curtain, you would probably observe the merging of 2, 3 and very rarely 4 folds, some folds remaining almost unaltered. We will however make the assumption, first proposed by mathematicians Jin and Sternberg, that the observed morphology can be described by successive period-doubling transitions (Jin et al. 2001). The global hierarchy is obtained by stitching these building-blocks. The key feature of a single block, named wrinklon, is its length, L, i.e., the sheet length required to accommodate the $\lambda - 2\lambda$ transition. This length should be determined by material properties, E, h the constraint/compression ratio δ and the wavelength. The power law describing self-similar patterns is then obtained from the relation

$$\frac{d\lambda}{dx} \sim \frac{\lambda}{L}$$

In fact, close inspection of the wrinklon morphology reveals the occurrence of a curved ridge at the tip of the merging folds (Fig 3.7). Such curved ridge is characterized by a non vanishing Gauss curvature. From the *Theorema Egregium*, the sheet around these curved ridge should concentrate stretching energy (i.e., the surface is no more isometric of a flat surface). The length of these elementary building-block can be obtained from energy minimization. The energy terms involved into a single $\lambda - 2\lambda$ transition should be related to local stretching, bending and the curved fold.

The stretching energy can be estimated from the slope of the sheet which determines the strain ϵ induced by the change of amplitude $A - 2A$ (related to the change of wavelength since $A \sim \sqrt{\delta}\lambda$). For a wrinklon of size $L\lambda$, the strain is given by $\epsilon \sim A^2/L^2 \sim \delta\lambda^2/L^2$ which yields the stretching energy

$$u_s \sim Eh \, L\lambda \, \epsilon^2 \sim Eh\delta^2\lambda^5 L^{-3}$$

The energy focalized in a curved fold was extensively studied by Pogorelov (1988) and later by Pauchard (1997),

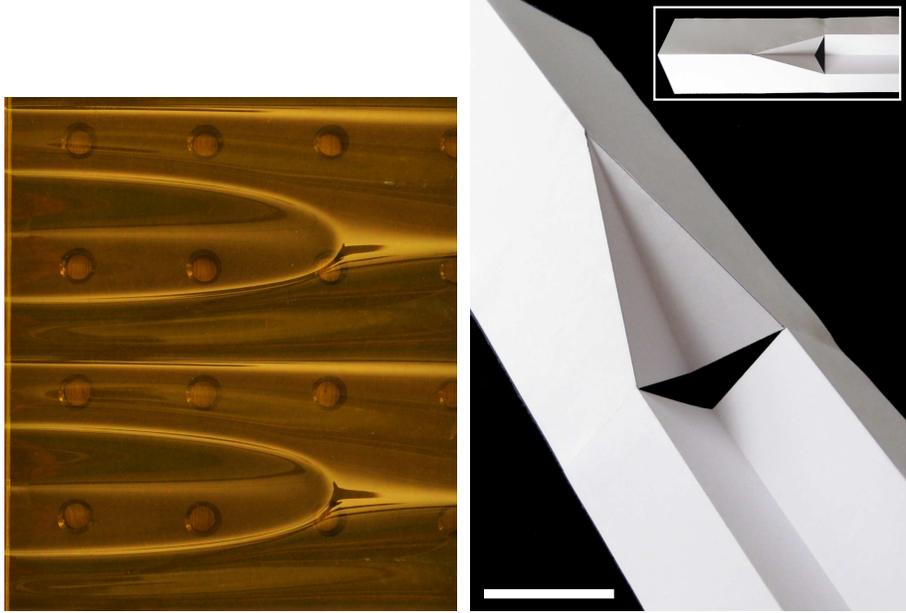$$u_c \sim Eh^{5/2} \, \alpha^{5/2} \, \rho^{1/2}$$

Fig. 3.7 (a) Wrinklon morphology. (b) Origami model of the $\lambda - 2\lambda$ transition (Vandeparre et al. 2011).

where α and ρ are the change of slope at the ridge and the radius of curvature of the fold, respectively. Since $\alpha \sim A^2/L^2$ and $\rho \sim \lambda^2/L$ (assuming a parabolic shape for the curved fold), this energy becomes

$$u_c \sim E h^{5/2} \ \delta^{5/4} \ \lambda^{7/2} L^{-3}$$

This energy term is however negligible compared to stretching energy since $u_c/u_s \sim (h/A)^{3/2} \ll 1$. The wrinklon morphology results then from a balance of stretching and bending energy, $u_b \sim E h^3 \ L\lambda\kappa^2$ which yields the length of a single building-block

$$L(\lambda) \sim h^{-1/2}\delta^{1/4}\lambda^{3/2}$$

The scaling for the wavelength describing the whole hierarchical pattern of folds is obtained by the integration of equation $d\lambda/dx \sim \lambda/L$, and is found to be,

$$\frac{\lambda(x)\delta^{1/6}}{h} \sim \left(\frac{x}{h}\right)^{2/3}$$

The class of patterns related to "light" curtains is in close agreement with this scaling, $\lambda \propto x^{2/3}$. In addition to yielding the proper exponent, this relation enables the comparison of the data obtained from seemingly disparate systems, over a wide range of lengthscales and independently of material properties. Fig 3.8 provides a remarkable collapse of the data measured with paper, fabric and various plastic sheets.
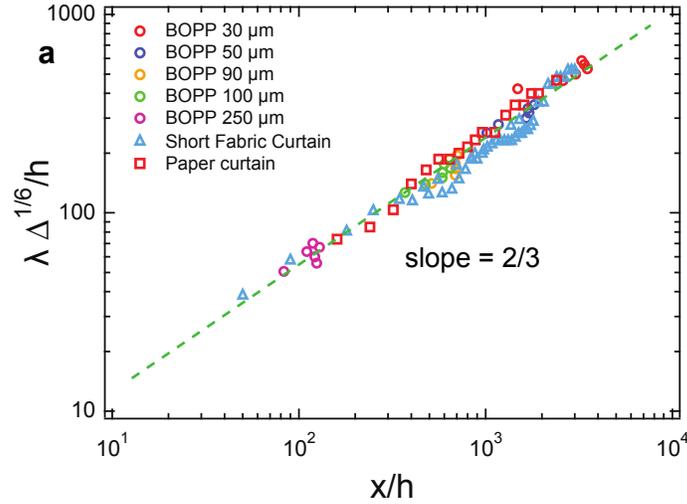
Fig. 3.8 Master curves, normalized wavelength vs normalized distance from edge for the "light" curtains (Vandeparre et al. 2011).
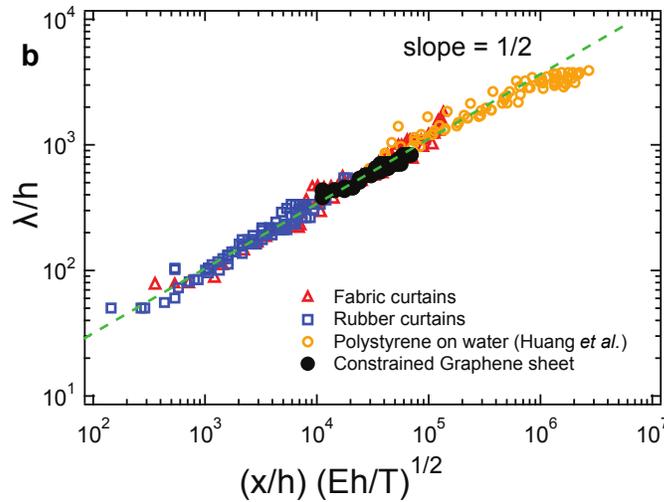

Fig. 3.9 Master curves, normalized wavelength vs normalized distance from edge for the "heavy" curtains (Vandeparre et al. 2011).

As shown in Fig. 3.6, "heavy" curtains, made of nanometric films of polystyrene on water (Huang et al. 2010), rubber sheets, and constrained graphene do not follow the 2/3 scaling. instead, their dynamics obey $\lambda \propto \sqrt{x}$). The main difference between both families is related to the lack or occurrence of a significant tensile force, T. For all "heavy" curtains, an additional tensile force is acting on the sheet. For graphene

sheets, this tension is related to the longitudinal tensile strain induced by thermal manipulations of the compression device (Bao et al. 2009). For rubber curtains, the tension is determined by gravity ($T \sim \rho_c g h H$, where ρ_c and H are the density and height of the curtain). For compressed nanometric polystyrene films on water, a tensile force is exerted by the surface tension of water at the free edges of the polymer film (Huang et al. 2010).

The tension per unit width, imposes an additional stretching energy given by,

$$U_t \sim T\,\alpha^2\,L\lambda \sim T\delta\lambda^3 L^{-1}$$

where α is the slope of the sheet within the wrinklon ($\alpha \sim A^2/L^2$).

This energy becomes dominant when $U_t > U_s$, that is when $T > Eh^2\delta/A$. Neglecting the stretching term, the total energy of the distorted membrane becomes $U_{tot} = U_t + U_b$. The length of a wrinklon which minimizes U_{tot} (balancing tension and bending energies) is given by,

$$L(\lambda) \sim \frac{\lambda^2}{h}\sqrt{\frac{T}{Eh}}. \tag{3.1}$$

As expected, the tensile force increases the length of wrinklons for a given wavelength and can thus be used to tune the energy penalty associated to $\lambda - 2\lambda$ transitions. Considering the equation $d\lambda/dx \sim \lambda/L$ with $L(\lambda)$ given by Eq 3.1, we obtain the scaling for the wavelength along a heavy sheet

$$\frac{\lambda(x)}{h} \sim \left(\frac{Eh}{T}\right)^{1/4}\left(\frac{x}{h}\right)^{1/2}. \tag{3.2}$$

This scaling is in excellent agreement with the power laws observed for heavy curtains and graphene bilayers, (Fig 3.6). The data of various macroscopic curtains, graphene bilayers and nanometric polystyrene thin films indeed collapse onto a single master curve without any fitting parameters (see Fig 3.9) which highlight the universality of our description. Our formalism is thus validated for 7 orders of magnitude in thickness from graphene sheets to rubber and fabric curtains.

3.3   Conclusions

In addition to the ridge and point-like singularities used to describe the crumpling of elastic sheets, diffuse stretching domain should be considered. Due to geometrical constraints that do not fill the "origami rules", the self-similar patterns of folds observed in curtain-like sheets are built by stitching together building-blocks, called wrinklons characterized by a diffuse stretching energy. The self-similar structure is then related to the size of the $\lambda - 2\lambda$ transition that depends on material properties and the local wavelength.

This example gives a little bit of flavor to the emergent research field related to constrained elastic sheets, where wrinkles, creases, sharp folds, crumples, wrinkle-to-fold transition and period-doubling bifurcation meet.

References

Audoly, B.; Pomeau, Y. (2010). *Geometry and Elasticity*. Oxford University Press, Oxford.

Baumchen, O.; Jacobs, K. (2010). Slip effects in polymer thin films. *J. Phys.: Condens. Matter*, **22**, 033102–21.

Baumchen, O.; Fetzer, R.; Jacobs, K. (2009). Reduced Interfacial Entanglement Density Affects the Boundary Conditions of Polymer Flow. *Physical Review Letters*, **103**, 247801–4.

Bao, W.; Miao, F.; Chen, Z.; Zhang, H.; Jang, H.; Dames, C.; Lau, C.N. (2009). Controlled ripple texturing of suspended graphene and ultrathin graphite membranes. *Nature nanotechnology*, **4**, 562–566.

Becker, J.; Grun, G.; Seeman, R.; Mantz, H.; Jacobs, K.; Mecke, K.; Blossey, R. (2003).Complex dewetting scenarios captured by thin-film models. *Nature Materials*, **2**, 59–63.

Blair, D.L.; Kudrolli, A. (2005). Geometry of crumpled paper. *Physical Review Letters*, **94**, 166107–4.

Bocquet, L.; Charlaix, E. (2010). Nanofluidics, from bulk to interfaces. *Chemical Society Reviews*, **39**, 1073–1095.

Bonn, D.; Eggers, J.; Indekeu, J.; Meunier, J.; Rolley, E. (2009). Wetting and spreading. *Review of Modern Physics*, **81**, 739–805.

Brau, F.; Vandeparre, H.; Sabbah, A.; Poulard, C.; Boudaoud, A.; Damman, P. (2010). Multiple-length-scale elastic instability mimics parametric resonance of nonlinear oscillators. *Nature Physs*, **7**, 56–60.

Cai, S.; Suo, Z.G.; Hayward, R.C. (2012). Creasing instability of elastomer films. *Soft Matter*, **8**, 1301–1304.

Coppée, S.; Geskin, V.M.; Lazzaroni, R.; Damman, P. (2004). Formation of Nanostructured Polymer Surfaces from Combined Relaxation and Crystallization. *Macromolecules*, **37**, 244–247.

Coppée, S.; Gabriele, S.; Jonas, A.M.; Jestin, J.; Damman, P. (2011). Influence of chain interdiffusion between immiscible polymers on dewetting dynamics. *Soft Matter*, **7**, 9951–9955.

Damman, P.; Baudelet, N., Reiter, G. (2003). Dewetting near the Glass Transition: Transition from a Capillary Force Dominated to a Dissipation Dominated Regime. *Physical Review Letters*, **91**, 216101–4.

Damman, P.; Gabriele, S.; Coppée, S.; Desprez, S.; Villers, D.; Vilmin, T.; Raphaël, E.; Hamieh, M.; Al Akhrass, S.; Reiter, G. (2007). Relaxation of Residual Stress and Reentanglement of Polymers in Spin-Coated Films. *Physical Review Letters*, **99**, 036101–4.

Debrégeas, G.; de Gennes, P.G.; Brochard-Wyart, F. (1998). The Life and Death of Bare Viscous Bubbles. *Science*, **279**, 1704–1707.

de Gennes, P.G. (1985). Wetting: static and dynamics. *Review of Modern Physics*, **57**, 827–863.

de Gennes, P.G.; Brochard-Wyart, F.; Quéré, D. (2003). *Gouttes, bulles, perles et ondes.* Belin, Paris.

Gabriele, S.; Sclavons, S.; Reiter, G.; Damman, P. (2006). Disentanglement Time of Polymers Determines the Onset of Rim Instabilities in Dewetting. *Physical Review Letters*, **96**, 156105–4.

Huang, J.; Davidovitch, B.; Santangelo, C.D.; Russell, T.P.; Menon, N. (2010). Smooth Cascade of Wrinkles at the Edge of a Floating Elastic Film. *Physical Review Letters*, **105**, 038302–4.

Jin, W.; Sternberg, P. (2001). Energy estimates for the von Krmn model of thin-film blistering. *Journal of Mathematical Physics*, **42**, 192–200.

Lobkovsky, A.; Gentges, S.; Li, H.; Morse, D.; Witten, T.A. (1995). Scaling Properties of Stretching Ridges in a Crumpled Elastic Sheet. *Science*, **270**, 1482–1485.

Pauchard, L.; Pomeau, Y.; Rica, S. (1997). Déformation des coques élastiques. *C. R. Acad. Sci. Paris*, **324**, 411–418.

Pogorelov, A.V. (1988). *Bendings of Surfaces and Stability of Shells*. Translations of Mathematical Monographs Vol. 72 (American Mathematical Society, Providence).

Redon, C.; Brochard-Wyart, F.; Rondelez, F. (1991). Dynamics of dewetting. *Physical Review Letters*, **66**, 715–718.

Reiter, G. (1992). Dewetting of Thin Polymer Films. *Physical Review Letters*, **68**, 75–78.

Reiter, G.; Khanna, R.; Sharma, A. (2000). Enhanced Instability in Thin Liquid Films by Improved Compatibility. *Physical Review Letters*, **85**, 1432–1435.

Reiter, G.; Khanna, R. (2000). Real-Time Determination of the Slippage Length in Autophobic Polymer Dewetting. *Physical Review Letters*, **85**, 2753–2756.

Rubinstein, ; Colby, . (2003). *Polymer Physics*. Oxford University Press, Oxford..

Sferraza, M.; Xiao, C.; Jones, R.A.L.; Bucknall, D.G.; Webster, J.; Penfold, J. (1997). Evidence for Capillary Waves at Immiscible Polymer/Polymer Interfaces. *Physical Review Letters*, **78**, 3693–3696.

Vandeparre, H.; Pineirua, M.; Brau, F.; Roman, B.; Bico, J.; Gay, C.; Bao, W.; Lau, C.N.; Reis, P.M.; Damman, P. (2011). Wrinkling Hierarchy in Constrained Thin Sheets from Suspended Graphene to Curtains. *Physical Review Letters*, **106**, 224301–4.

Vella, D.; Ajdari, A.; Vaziri, A.; Boudaoud, A. (2011). Wrinkling of Pressurized Elastic Shells. *Physical Review Letters*, **107**, 174301–4.

Vilmin, T.; Raphaeil, E. (2006). Dewetting of thin polymer films. *Eur. Phys. J. E*, **21**, 161–174.

Vilmin, T. (2006). Quelques Propriétés des Polymères en Couches Minces *Thèse de doctorat*. Université Paris 6

Witten, T.A. (2007). Stress focusing in elstic thin sheets. *Review of Modern Physics*, **79**, 643–675.